Egypt. J. Chem. **Vol. 65,** No. SI: 13B pp. 119 - 136 (2022)

Egyptian Journal of Chemistry

http://ejchem.journals.ekb.eg/

Photodeposited Silver versus Gold over g-C_3N_4 toward Photocatalytic Oxidation of Organic Water Pollutants

Mostafa Zedan [a,b], Xu Li [b,c,d,*], Rehab M. Amin [a], Souad A. ElFeky [a], Abdallah F. Zedan [a,*]

[a] *National Institute of Laser Enhanced Science, Cairo University, Giza, 12613, Egypt.*

[b] *Institute of Materials Research and Engineering, Agency for Science, Technology and Research (A*STAR), Singapore 138634, Singapore.*

[c] *Institute of Sustainability for Chemicals, Energy and Environment, A*STAR, Singapore 627833, Singapore.*

[d] *Department of Food Science & Technology, National University of Singapore, Singapore 117543, Singapore.*

Abstract

Water is a valuable reserve that shall be efficiently treated for sustainable growth and development. Metal nanoparticles (MNPs) and graphitic carbon nitride (gCN) have received immense attention for several applications. In this paper, the facile synthesis of MNPs/gCN hybrid photocatalysts based on sonodispersion, and *in-situ* reduction and photodeposition is described. Photodeposition of two different metals, namely gold nanoparticles (Au NPs) and silver nanoparticles (Ag NPs) with different loading ratios was studied. The morphological, structural, electronic, optical, and surface properties of the prepared catalysts were investigated. The photocatalytic activity of the prepared catalysts was evaluated for photooxidation of organic water pollutants under visible light irradiation using methyl orange (MO) and rose bengal (RB) as model dyes. The photo- and recycling stability, and the photoelectrochemical properties of a selected photocatalyst were also studied. The results confirmed the evident formation and characteristics of the prepared MNPs/gCN materials. The catalysis measurements revealed the promoting effect of the Au and Ag NPs toward the adsorptive removal and photooxidation of MO and RB. Overall, the Ag NPs demonstrated higher catalytic activity for dye oxidation compared to Au NPs. The Au/gCN resulted in adsorptive removal of 3.87-11.80 % of MO, whereas the Ag/gCN led to adsorptive removal of 66.45-85.33% of MO within 1 h in dark. Also, Ag/gCN catalysts exhibited an extraordinary adsorption ability toward RB that is six-time higher than that of Au/gCN. Interestingly, the Ag/gCN photocatalysts demonstrated the highest photocatalytic activity with 100% photooxidation of MO, and RB within 20 min, and 15 min under visible light irradiation, respectively. The high photocatalytic activity could arise from the coupled plasmon absorption, enhanced visible light harvesting, and efficient charge separation. Besides superior photocatalytic activity, the Ag/gCN catalyst expressed promising photostability, reusability, and photoelectrochemical responses. The obtained results indicate that MNPs/gCN materials could serve as efficient visible-light-sensitive catalysts for photocatalytic water treatment.

Keywords: Photodeposition; Photodegradation; Catalysis; Metal Nanoparticles; Carbon.

1. Introduction

The global environmental crises including water pollution and the shortage of energy are becoming progressively worse, due to the rapid growth of the population and the fastest modernization.[1] As a result, one of the most vital challenges is how to guarantee safe and clean accessible water. Water is considered the most valuable reserve among all-natural resources that should be conserved, treated, and cleaned in an efficient way for sustainable growth.[2] The control of water pollution is one of the big challenges in front of the scientific community with its main concern for the protection and conservation of natural water resources. Among a variety of water pollutants, organic dyes are the most common category that is discharged in industrial and municipal wastewater sources. The unrestrained discharge of these pollutants causes severe environmental contamination, increases the water crisis, and hence harms plants, animals, and human beings.[3, 4] Consequently, several technologies have aroused and gained great interest in the removal of water pollutants to overcome these hazards. The current conventional technologies for water treatment still do not meet the required ideal.[5] Therefore, there is a pressing necessity to develop a non-conventional,

*Corresponding authors e-mail: zedanabdallah@cu.edu.eg.; (Abdallah F. Zedan); x-li@imre.a-star.edu.sg, (Xu Li).

Receive Date: 20 January 2022, Revise Date: 18 April 2022, Accept Date: 27 April 2022

DOI: 10.21608/EJCHEM.2022.117227.5293

sustainable, efficient, and green technology for water treatment.

Photocatalysis offers one of the most promising technologies in environmental remediation applications that utilize renewable solar energy. It has gained great attention in water pollutants elimination and solar energy conversion due to its effectiveness and sustainability.[6] Besides, solar energy is the most desirable resource for environmental decontamination and energy conversion due to its abundance, renewability, and ecofriendly.[7] Semiconductor photocatalysis has become an ideal approach to tackling global environmental issues using semiconducting-based materials owing to their unique performance in solar energy utilization and environmental applications.[6] Additionally, it is an eco-friendly, economic, safe, renewable, and clean technology in various applications, which conduct catalytic reactions such as the removal of water pollutants.[8] Up to now, there are numerous traditional semiconductors have been reported in the literature and were designed for photocatalytic degradation processes such as TiO_2, WO_3, and ZnO.[9] However, these photocatalysts have some drawbacks/obstacles such as the wide bandgap and are only active under UV irradiation, which limits the photocatalytic performance. Over recent years, the polymeric metal-free that originated from elemental semiconductors and a variety of carbon-based materials has received immense research interest as a potential photocatalyst.[10]

Of particular interest, graphitic carbon nitride (g-C_3N_4 or gCN) has gained great excitement in the scientific community as a promising polymeric metal-free photocatalyst. Pristine gCN possesses several outstanding properties including, a narrow optical bandgap (2.7 eV), high chemical, physical and thermal stability, simple preparation, earth-abundant, and non-toxicity. Thus, the gCN has become a favorable photocatalyst in environmental remediation applications such as photooxidation of water organic pollutants.[10-13] Nevertheless, the pristine gCN has a limited photocatalytic activity owing to the rapid recombination of the photogenerated charge carriers, namely the electron/hole pairs, the low active sites over the surface, and insufficient sensitivity for the visible light absorption.[14] To address these challenges, several strategies such as surface defects [15, 16], metal doping [17, 18], nonmetal doping [16, 19], conjugation with other semiconductors [20, 21], and construction of various nanostructures [22, 23] have been applied to improve the photocatalytic properties of pristine gCN and thus expand its practical applications.

The deposition of metal nanoparticles (MNPs) as a co-catalytic system onto the gCN surface is an efficient approach for the improvement of the photocatalytic activity of pristine gCN. The MNPs coupled with semiconductor can stimulate the localized surface plasmon resonance (LSPR) effect and causes a redshift of its optical absorption properties. The deposited MNPs on gCN have been shown to improve light harvesting and decrease the recombination rate of the photogenerated charge carriers.[14, 24, 25] The co-catalytic MNPs act as active reaction sites which increases the visible light absorption and promotes the separation of the photogenerated electrons and holes.[18] Several reports have studied the performance of different metal/ gCN hybrids synthesized using a variety of approaches such as anion-exchange [26], precipitation [27], solvothermal [28], hydrothermal [29], impregnation [30], electrodeposition [31], atomic layer deposition [32], sputtering [33], and biogenic synthesis.[34] Nevertheless, it is important to refer to that these techniques could suffer some limitations including quite lengthy reaction steps, consuming time and energy, using toxic chemicals or templates, the need for high potential or temperature, in addition to inhomogeneity encountered in the formed metal-loaded products.

On the other hand, the ultrasonication-induced synthetic methods have gained further attention for preparing the heterostructured metal/semiconductor photocatalysts. The utilization of ultrasonication waves for the deposition of MNPs can lead to a suitable nucleation process and good distribution of the particles onto the semiconductor surface.[35, 36] Faisal *et al.*, have loaded the Au NPs over the gCN surface by using an ultrasonication method and studied its photocatalytic activity for the degradation of water pollutants.[37] Moreover, Zhu *et al*., have prepared the Ag/gCN nanocatalysts via the chemical reduction and the ultrasonic irradiation in an inverter microreactor in presence of $NaBH_4$ as a reducing agent.[36] Even though the ultrasonication may stimulate the in-situ reduction of metal salt precursors over a semiconductor surface, the efficiency of the chemical reduction process is limited and is greatly affected by sonication and reaction parameters. The incorporation

and formation of such nanoparticles are subject to disturbing by many variables during the ultrasonication process such as the ultrasound frequency and power, the processing time, the mode of sonication process. One may also need to carry out the ultrasonication in presence of some reducing agents to ensure the complete reduction of precursors, which could yield undesired impurities in the final product.[36, 38]

As an alternative, the photodeposition method has been widely studied for the synthesis of a variety of photocatalyst nanomaterials due to its effectiveness in preparing well-defined metal nanoparticles attached to semiconductor surfaces. Several hybrid nanostructures were prepared by the photodeposition method for different applications such as environmental remediation and water treatment.[14, 39] The efficiency of the photodeposition process depends largely on optimizing the photodeposition conditions including the solution pH, the atmosphere, and the sacrificial agents. Sometimes, post-synthesis high-temperature treatment or prolonged UV treatment is performed for removal of the remaining organics, which may alter the properties of the deposited particles.[39] The photocatalytic properties of the heterostructures are greatly affected by the photodeposition conditions. Therefore, the photodeposition scheme needs to be tailored toward achieving efficient particles dispersion, good surface distribution, and improved active sites.[40] In this regard, some attempts to explore synthetic approaches combining the deposition method with other methods to expand the advantages of the products have been reported.[35, 41-43] One example is the sono-photodeposition approach that combines photodeposition and ultrasound waves in one simultaneous step. Colmenares *et. al*. adopted this approach to fabricate bimetallic systems of Pd-Au@TiO_2 for the photocatalytic oxidation of methanol.[41] Magdziarz *et. al.* developed a similar approach to synthesize iron-titania/zeolite photocatalysts for photocatalytic oxidation of benzyl alcohol using ultrasound waves assisted with visible light irradiation.[42] Moreover, Jodeyri *et al.*, have studied the photocatalytic performance of the Ag/gCN-clinoptilolite (Ag/C_3N_4-CLT_x) photocatalysts synthesized using sono-photoreduction dispersion toward the tetracycline degradation.[43]

In this work, we developed a sequential approach combining sonodispersion followed by *in-situ* photoreduction and deposition for the synthesis of MNPs/gCN. Two different types of noble metals, namely gold nanoparticles (Au NPs) and silver nanoparticles (Ag NPs) were photodeposited onto gCN. To study the effect of metal loading percentage, two series of *x*%Au/gCN and *x*%Ag/gCN with different Au and Ag weight ratios were prepared. The photocatalytic activity of the prepared photocatalysts for oxidation of organic water pollutants was studied using methyl orange and rose Bengal as model dyes. Our sequential synthesis method adopting sonodispersion and photoreduction enabled the uniform nucleation, reduction, and deposition of MNPs on the gCN sheets. The photodeposited catalysts were prepared without using any chemical reducing agents or organic stabilizers to avoid catalyst contamination. The method yielded catalysts with controlled size and good dispersion of MNPs over the gCN surface. The in-situ photoreduction and deposition of the MNPs (Au NPs and Ag NPs) over the gCN surface were confirmed by using several characterizations and analytical techniques including XRD, FTIR, TEM, SEM, XPS, BET surface area, UV-Vis DRS, and PL spectroscopy. A comparative study of the photocatalytic activities of the prepared photocatalysts for the photocatalytic oxidation of selected organic dyes under visible light irradiation was performed. Moreover, the photoelectrochemical properties of the selected photocatalyst were studied by the electrochemical impedance spectroscopy (EIS) and measurements of the photocurrent characteristics to compare the separation efficiency of photogenerated charges species. The overall catalysis measurements revealed the promoting effect of the photodeposited MNPs over the gCN surface.

2. Experimental

2.1. Materials

The chemicals and reagents were purchased and used without further purification or treatment. The chemicals included urea (99.0-100.5%, ACS reagent, Honeywell Fluka), tetrachloroauric acid trihydrate (≥99.9%, Sigma-Aldrich, Germany), silver nitrate (≥99%, Sigma-Aldrich, Germany), methanol absolute (≥99.8%, Sigma-Aldrich, Germany), methyl orange (MO, Sigma-Aldrich, Germany), and rose bengal (RB, Sigma-Aldrich, Germany).

2.2. Methods

2.2.1. Polycondensation Synthesis of Graphitic Carbon Nitride (gCN)

Graphitic carbon nitride (gCN) was prepared via the thermal polycondensation of urea under static air as reported in the literature with a slight modification.[34] Typically, a predetermined amount of urea was placed in a capped ceramic crucible and heated in a muffle furnace at 550 °C for 2 h with a heating rate of 10 °C/min in static air. Upon completion, the obtained yellowish powder of gCN was collected, and grounded into a fine powder that was used as is without any purification.

2.2.2. Synthesis of Au/gCN and Ag/gCN Nanostructured Photocatalysts

The Au/gCN and Ag/gCN nanostructured photocatalysts were synthesized a facile synthetic method involving the sonodispersion followed by in-situ photoreduction and deposition of the MNPs over the gCN surface, as illustrated in **Figure 1**. In a typical synthesis of MNPs/gCN, 1 g of the as-prepared gCN powder material was dispersed in 50 ml of deionized water in a 250 ml beaker. The mixture was ultrasonicated for 30 min, then a designated volume of methanol as a sacrificial agent was added followed by further ultrasonication for 30 min to obtain a homogeneous slurry. In both cases of Au/gCN and Ag/gCN, pre-designated volumes of aqueous solutions of $HAuCl_4$ ($5x10^{-2}$ M) and $AgNO_3$ **(**$3.5x10^{-3}$ M**)** were added to the aqueous gCN/methanol slurry. The slurry was ultrasonicated for 20 min followed by stirring for 1 h in dark. Then, the reaction mixture was subjected to UV irradiation using UV solar simulator (SOL2, Honle) under magnetic stirring for 30 min to allow in-situ photoreduction and deposition. Upon completion, the reaction products were centrifuged and washed with distilled water three times. Finally, the MNPs/gCN products were dried at 90 ^{o}C for 12 h and powder samples were kept for further analysis. The apparent colors of the reaction products in the case of Au/gCN and Ag/gCN were brownish-red and brownish, respectively. To study the effect of the metallic ratio on the catalytic activity, the weight ratio of metal precursor in the *x*%Au/gCN and *x*%Ag/gCN hybrids nanostructured was varied as *x*= 2 wt.% and 5 wt.%.

2.3. Characterization

The prepared pristine gCN and *x*% MNPs/gCN materials were characterized to study their morphologies, crystallinity, phase structure, chemical composition, optical, surface, and electronic properties using standard analytical techniques including SEM, TEM, XRD, FTIR, XPS, BET surface area, UV-Vis DRS and PL spectroscopy. Scanning electron microscope (SEM) images were collected using a JSM-6700F microscope (JEOL). Transmission electron microscope (TEM) images were obtained using a JEM-2100 microscope (JEOL). The powder X-ray diffraction (XRD) spectra were recorded on a D8-Advance (Bruker) adopted with Cu Kα radiation (1.5405 A°). The Fourier transform infra-red (FTIR) spectra were measured in the range of 600-4000 cm^{-1} wavenumbers using a Spectrum-2000 spectrometer (Perkin-Elmer). The X-ray photoelectron spectroscopy (XPS) measurements were carried out using Theta Probe (Thermo-Fisher Scientific) in an ultrahigh vacuum environment. All obtained XPS data were calibrated using C1s as reference peak at 284.5 eV. The nitrogen (N_2) adsorption-desorption isothermal plots of the prepared materials were obtained using the ASAP 2020MP programmed gas sorption analyzer (Micromeritics) at relative pressure ranging from 0.05 to 1. The BET-specific surface area (BET-SSA) and the pore size properties of the as-prepared samples were obtained from the isothermal data using the BET model and Barret-Joyner-Halenda (BJH) methods, respectively. The UV-Vis diffuse reflectance spectroscopy (UV-Vis DRS) measurements were carried out using an integrating sphere unit (ISR-603) attached to the UV-3600 (Shimadzu) spectrophotometer. The photoluminescence (PL) spectra of diluted samples suspension were recorded using an RF5301 spectrofluorophotometer (Shimadzu) equipped with a Xe-lamp as an exciting source. The zeta potential (ζ-potential) measurements of diluted samples were determined using a Nano-ZS90 (Malvern) Zetasizer at a 90° scattering angle.

2.4. Photocatalytic Oxidation of Organic Water Pollutants over MNPs/gCN

The photooxidation of organic pollutants reactions was applied to evaluate the photocatalytic performance of the synthesized photocatalysts. The photocatalysis measurements were performed using model dyes including MO (10 mg/L) and RB (20 mg/L) in an aqueous medium under visible light irradiation, as depicted in **Figure 1**. The experimental

parameters affecting the photocatalytic performance rate including catalyst loading and dye concentration were investigated. All photocatalytic measurements were performed in an ambient atmosphere under continuous magnetic stirring at room temperature. The visible light irradiation was provided using a 300 W Xe-lamp solar simulator (Newport-Oriel) that is equipped with a UV cut-off filter (Irradiance of 100 $mW.cm^{-2}$).

In a typical experiment, a certain amount of each photocatalyst was dispersed in an aqueous solution of MO (dosage; 1mg/ml) and RB (dosage; 0.5mg/ml), respectively. Then, before irradiation, the mixture was ultrasonicated for 10 min and stirred for 60 min in dark to attain the adsorption-desorption equilibrium. During the photooxidation experiment, different aliquots of the reaction mixture were taken at given interval times of irradiation. Then aliquots were taken and centrifuged twice for 10 min at 10000 rpm to remove the catalyst powder. The remaining concentrations of tested dyes for all experiments were measured using a UV-Visible spectrophotometer (UV-2450, Shimadzu) at λ_{max}=464 nm for MO and 549 nm for RB. The photooxidation efficiency percentage of each tested catalyst was estimated by using the following equation:

Photooxidation Efficiency (%) = [1-(C/C_0)] x100

Where C_0 and C are representing the initial and remaining concentration of tested dye at a definite time of exposure.

The reusability and photostability of selected photocatalyst were evaluated up to three catalyst cycles under visible light irradiation. For the reusability study, no aliquot samples were withdrawn during the photooxidation reaction. After each cycle, the catalyst was centrifuged and washed with a mixture of water and ethanol. Upon washing, it was centrifuged again and was finally left in an oven till drying for the next cycle.

2.5. Photoelectrochemical (PEC) Measurements

The PEC measurements were performed on an electrochemical workstation (VSP-300, Biologic system) that is equipped with a conventional three electrodes cell. The system consisted of an ITO substrate coated with catalyst paste as a working electrode, Pt wire as a counter electrode, and Ag/AgCl (3M, KCl) as a reference electrode, respectively. An aqueous solution of 0.1 M sodium sulfate (Na_2SO_4, pH ~7) was used as a supporting electrolyte in all PEC experiments. The working electrodes were illuminated using a Xe lamp (150 W, Newport-Oriel) fitted with AM 1.5 filter and a UV cut-off filter for the visible light (with an irradiance of 50 $mW.cm^{-2}$). The measurements of electrochemical impedance spectroscopy (EIS) were performed at 50 mV amplitude and over a frequency range from 0.1 Hz to 10^4 Hz. Moreover, the chronoamperometry (*I-t*) of all prepared photoelectrodes was tested for several on-off cycles in dark-light irradiation. All the PEC measurements were conducted in static air at room temperature. The ITO working electrode was prepared as follows; 4 mg of each catalyst powder was dispersed into 2 ml of ethanol and then mixed thoroughly with Nafion solution (400 µl) under ultrasonication for 10 min. Afterward, 10 µl of the slurry was dip-coating onto the conductive side of a cleaned ITO substrate (1cm x 1cm) and sintered at 80 ºC for 4 h.

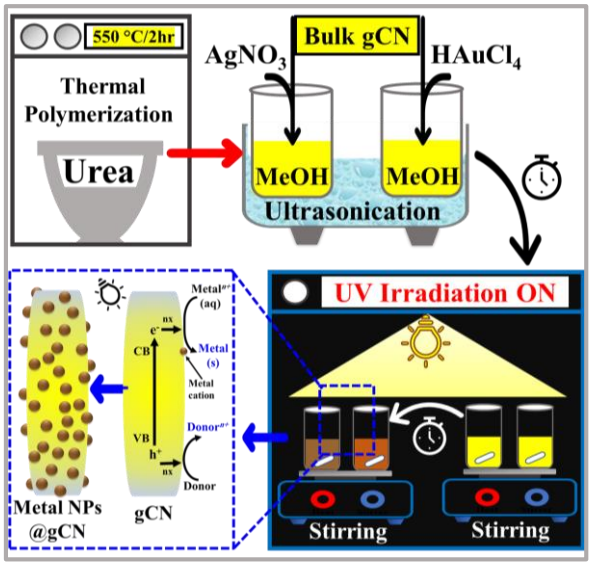

Figure 1. Schematic representation of the steps involved in the synthesis of gCN and the MNPs/gCN hybrids, and also a sketch of the in-situ photoreduction and deposition.

3. Results and Discussion

The synthesis of visible-light-driven photocatalysts based on the coupling of gCN and MNPs has been studied for different applications such as environmental remediation.[17, 18, 23, 24] These reports outlined that the coupling of MNPs with gCN structures can improve the photocatalytic characteristics of gCN in the visible region, for example in the photocatalytic degradation of water

pollutants. The effect of the MNPs is mainly related to the effective separation of the charge carriers upon photoexcitation of gCN. In this regard, it would be beneficial if the capability of the gCN to harvest visible light radiation could be extended. Herein we show that the decorating of the surface of gCN with MNPs (Au and Ag) as cocatalyst could enable achieving better charge separation and also introduce visible-light sensitivity for oxidation of organic water pollutants.

3.1. Morphological and Structural Properties

The gCN was prepared from urea by using the thermal polycondensation method at 550 °C for 2 h. The as-prepared gCN was used as support for the deposition of different loadings of MNPs (Au or Ag) using the sonodispersion followed by in-situ photoreduction as described above. To study the effect of metal ratio in the final MNPs/gCN composite on photocatalytic activity, a series of *x*%Au/gCN and *x*%Ag/gCN hybrid photocatalysts with different Au and Ag ratios were fabricated. The metal loading ratio of the different Au/gCN and Ag/gCN photocatalysts was varied as 2 wt.% and 5 wt.%. **Figure 2** displays the FE-SEM of gCN and the HR-TEM of gCN, 5%Au/gCN, and 5%Ag/gCN photocatalysts. The FE-SEM image of pristine gCN (**Figure 2-a**) indicates agglomerated and layered nature of the gCN with lateral dimensions of several micrometers. Also, the HR-TEM image of gCN (**Figure 2-b)** reveals the irregular shape of gCN with aggregated layers. The HR-TEM images of the prepared 5%Au/gCN and 5%Ag/gCN composite photocatalysts are presented in **Figure 2-c,d**. The HR-TEM images indicate the formation and anchoring of the semi-spherical shaped MNPs of an average size of 20±5 nm on gCN sheets. They also confirm that the Au NPs (~20±5 nm) and Ag NPs (~20±5 nm) are well distributed on the surface of the gCN layers. The good anchoring of the MNPs onto the gCN can improve the visible light absorption and promote the photocatalytic performance under visible light irradiation as will be explained in the following sections.

The phase structure of the prepared catalysts including pristine gCN, Au/gCN, and Ag/gCN were studied using X-ray diffraction (XRD) spectroscopy at room temperature. **Figure 3** compares the XRD patterns of gCN, 2%Au/gCN, 5%Au/gCN, 2%Ag/gCN, and 5%Ag/gCN powder photocatalysts. The XRD pattern of gCN **(Figure 3-a)** shows two XRD peaks at 2θ values of 12.75° and 27.4° that correspond to the (100) and (002) crystal planes of the gCN, respectively. The obtained XRD pattern confirms the graphitic stacking phase of gCN as reported before.[15, 16] The XRD patterns of Au/gCN and Ag/gCN hybrid photocatalysts with different metal ratios of 2 wt.% and 5 wt.% (**Figure 3-b-e**) overall reveal XRD diffraction peaks characteristic to both gCN and MNPs.

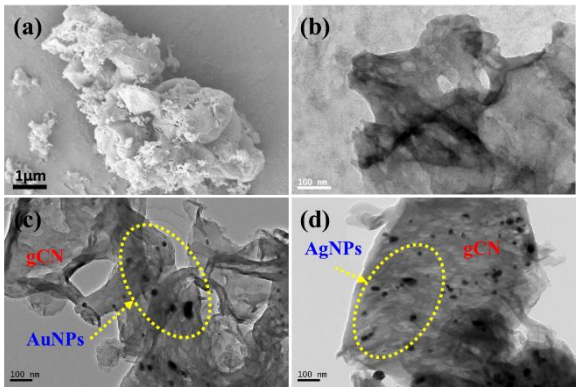

Figure 2. (a) FE-SEM of gCN. **(b-d)** HR-TEM of **(b)** gCN, **(c)** 5%Au/gCN, and **(d)** 5%Ag/gCN photocatalysts.

For the 2% and 5%Au/gCN photocatalysts **(Figure 3-b,c)**, the XRD patterns are featured with diffraction peaks at 2θ values of 38.06º, 44.05º, 64.45º and 77.62º associated with the crystal planes (111), (200), (220) and (311) of Au NPs with a face-centered cubic (fcc) structure, respectively. In the case of 2% and 5% Ag/gCN photocatalysts **(Figure 3-d,e)**, the XRD patterns exhibit additional two diffraction peaks alongside the characteristic peaks of gCN. The additional diffraction peaks at 2θ values of 38.06º and 44.05º can be attributed to the (111) and (200) crystal planes of the fcc Ag NPs, respectively. The diffraction peaks of the Au/gCN and Ag/gCN hybrids are consistent with literature values reported for Au NPs (JCPDS# 04-0784) [44], and Ag NPs (JCPDS# 04-0783).[45]

The XRD peaks associated with the MNPs express systematic variation of the peak intensity with metal loading composition. The relative intensity of the MNPs increases with the nominal weight ratio of the MNPs in the different photocatalysts. This indicates the uniform formation of the hybrid catalysts with metallic ratios comparable to experimentally-used amounts. There is no other diffraction peaks are observed in the different MNPs/gCN hybrids,

indicating the pure phase of the gCN and lacking any impurities during the fabrication of the Au/gCN and Ag/gCN photocatalysts. The XRD data also confirm that the crystal structure and the inter-planer stacking arrangement of gCN remained unaltered after the sonodispersion and photodeposition processes.

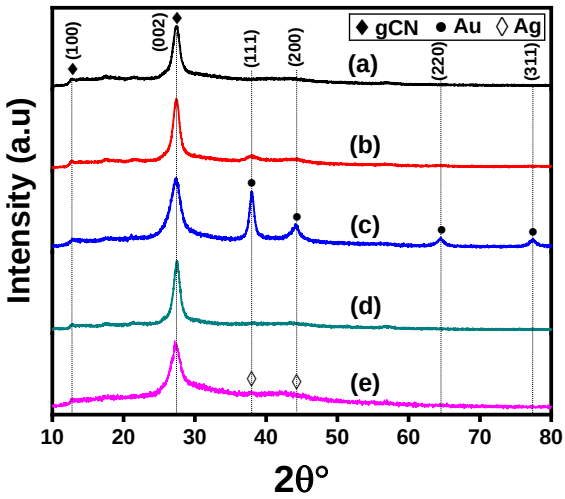

Figure 3. XRD patterns of **(a)** gCN, **(b)** 2%Au/gCN, **(c)** 5%Au/gCN, **(d)** 2%Ag/gCN, and **(e)** 5%Ag/gCN powder samples.

3.2. Electronic Properties

FTIR spectroscopy is a strong tool to study the chemical and electronic structure and vibrational characteristics of materials and confirm lattice properties.[46-48] The FTIR spectra of the prepared gCN and MNPs/gCN were collected to reveal the electronic characteristics of the different catalysts. **Figure 4** presents the FTIR spectra of gCN, 2-5%Au/gCN, and 2-5%Ag/gCN samples in the wavenumber range of 500-4000 cm^{-1}. The FTIR spectra of the gCN and different MNPs/gCN hybrid photocatalysts exhibit similar electronic vibrational characteristics. The broad FTIR band in the range of 3000-3675 cm^{-1} can be assigned to the stretching (N-H) vibrational modes of the uncondensed amino groups and the adsorbed hydroxyl (O-H) groups from water molecules existing on the gCN surface. The strong absorption bands from 1245 cm^{-1} to 1640 cm^{-1} wavenumber can be ascribed to the typical aromatic stretching modes of (C-N) heterocycles. Additionally, the intense absorption band positioned at 810 cm^{-1} indicates the characteristic mode of the tri-*s*-triazine rings.[20, 49] Clearly, these findings further reveal that the chemical structure and crystallinity of gCN are maintained throughout the entire sonodispersion/photodeposition process, which is consistent with the XRD results.

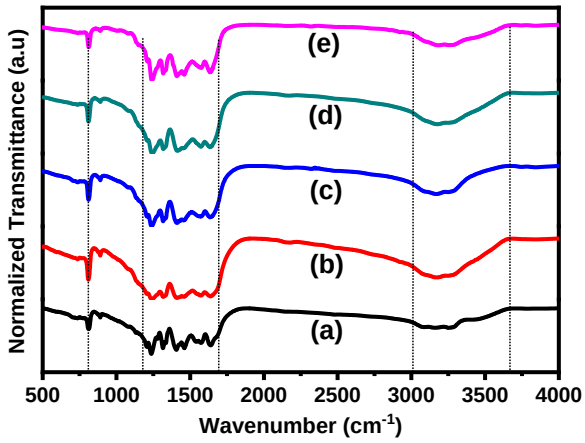

Figure 4. FTIR spectra of **(a)** gCN, **(b)** 2%Au/gCN, **(c)** 5%Au/gCN, **(d)** 2%Ag/gCN, and **(e)** 5%Ag/gCN catalysts.

3.3. Surface Properties

The nitrogen (N_2) adsorption-desorption isothermal plots were measured to investigate the specific surface area (BET-SSA) of gCN, 5%Au/gCN, and 5%Ag/gCN samples. The plots of the adsorbed quantity versus relative pressure (P/P_0) and the pore volume of the measured samples are shown in **Figure 5** and the inset graph. The estimated BET-SSA of the studied samples were 45.02, 22.94, and 53.23 m^2/g, for gCN, 5%Au/gCN, and 5%Ag/gCN, respectively. Materials offering a high specific surface area (SSA) are known to express a larger number of active sites on the catalyst surface and this can promote catalytic activity.[50-52] The gCN showed a BET-SSA of 45.02 m^2/g whereas a 5%Ag/gCN hybrid exhibited a higher BET-SSA of 53.23 m^2/g. The larger SSA of the 5%Ag/gCN hybrid compared to pristine gCN reveals the effect of the small-sized Ag NPs on the SSA, which is desired for high catalyst activity. [6] The large surface area of a catalyst can increase the number of adsorbed reacting species on the surface. It can also increase the number of photogenerated charges (electrons and holes) improving photocatalytic performance. Meanwhile, the 5%Au/gCN expressed a low BET-SSA of 22.94 m^2/g which is smaller than that of gCN and this can be ascribed to lowering the porous nature of gCN with metallic nanoparticles that exhibit low porosity.[37, 53] The small SSA of the MNPs/gCN compared to gCN can be attributed to the possible interparticle agglomeration that occurs after the metal deposition, which can block some pores and

fill some spaces over the gCN surface. The data obtained on the BET-SSA, Barret-Joyner-Halenda (BJH) pore volume, and pore size of gCN, 5%Au/gCN, and 5%Ag/gCN are summarized in **Table 1**. As can be seen in the inset graph in **Figure 5** and also as listed in **Table 1**, the average BJH-pore size of the different hybrids significantly improved compared to gCN. These results revealed that the anchoring of MNPs had a synergistic effect on the BET-SSA and the porosity nature of the MNPs/gCN hybrid photocatalysts.

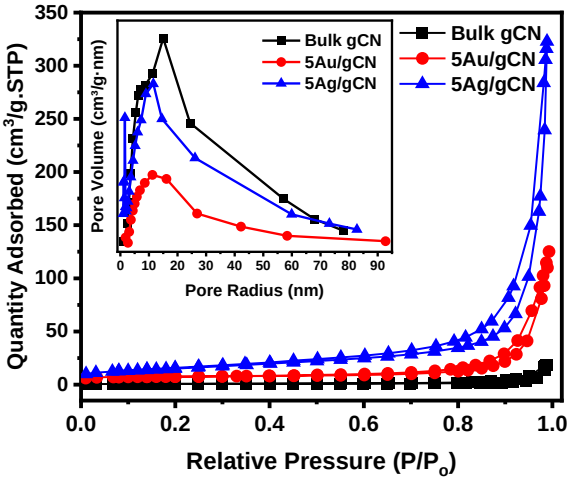

Figure 5. Nitrogen (N_2) adsorption-desorption isothermal plots and (inset) the BJH-pore size distribution of gCN, 5%Au/gCN, and 5%Ag/gCN powder photocatalysts.

The XPS analysis is very helpful to study the surface properties and reveal the valence electronic state of chemical species. Thus, survey and high-resolution XPS spectra were measured to study and characterize the prepared samples including gCN and MNPs/gCN hybrid photocatalysts. **Figure 6-a** displays the low-resolution survey XPS spectra recorded for gCN, 5%Au/gCN, and 5%Ag/gCN samples. The XPS survey spectra confirm the existence of two major peaks assigned to C 1s and N 1s and a small peak for O 1s. In addition, the spectra of 5%Au/gCN and 5%Ag/gCN samples reveal features characteristic of Au and Ag, respectively.[25] The three full-range surveys XPS spectra (**Figure 6-a**) confirm the characteristic features of the C 1s and N 1s of gCN and hybrid MNPs/gCN materials. The differences of the XPS spectral properties of gCN after modification with Au NPs or Ag NPs reveal the co-existence of metal peaks (Au 4f and Ag 3d) and confirms the formation of *x*%Au/gCN and *x*%Ag/gCN nanostructures. **Figure 6-b-d** and **Figure 7-a-b** display the high-resolution XPS spectra obtained for C 1s, Au 4f, Ag 3d, N 1s, and O 1s of selected photocatalysts are presented in. **Figure 6-b** compares the C 1s fitted spectra of the gCN, 5%Au/gCN, and 5%Ag/gCN samples that were measured in the scan range of 282-294 eV and are showing two major peaks. The two distinct XPS peaks of C 1s for gCN are centered at 284.50 eV and 287.98 eV, respectively. The weak peak can be ascribed to the aromatic C atom in the rings of tri-*s*-triazine units and the strong peak indicates the hybridized C atom in sp^2 (N-C=N) or (C-C).[49, 53] It can be noticed that the strong peak position of C 1s is shifted to a higher value of binding energy in the case of 5%Au/gCN (288.31 eV) and 5%Ag/gCN (288.41 eV) hybrids compared to that of pristine gCN confirming interaction of the Ag metal with gCN. The strong coupling could result in higher charge separation and enhanced catalytic activity of MNPs/gCN.[8] **Figure 6-c** displays the XPS spectrum of Au 4f for 5%Au/gCN sample showing two distinct peaks located at 83.47 eV and 87.17 eV that are ascribed to Au $4f_{7/2}$ and Au $4f_{5/2}$ core levels, respectively. This indicates that the Au^{3+} ions were reduced onto the gCN surface to the Au^0 oxidation state.[17] on the other hand, the XPS fitted spectrum of the Ag 3d for 5%Ag/gCN (**Figure 6-d**) can be deconvoluted into two separate strong peaks at 368.47 eV and 374.51 eV, respectively. The XPS peak at 367.88 eV can be attributed to the core level of Ag $3d_{5/2}$ and that positioned at 373.87 eV can be ascribed to Ag $3d_{3/2}$ core level.[25] **Figure 7-a** displays the XPS spectra of N 1s for the gCN, 5%Au/gCN, and 5%Ag/gCN samples. The fitted spectra of selected samples (**Figure 7-a**) have four major characteristic peaks for N 1s located at 398.48 eV, 399.55 eV, 401.02 eV, and 404.26 eV binding energies, respectively. The main strong peak at 398.48 eV may be originated from the hybridized aromatic N atom of (SP^2) C-N=C, which indicates the presence of *s*-triazine rings. While the other three peaks can be attributed to the tertiary N atoms of (N-$(C)_3$), (N-H) groups or (C-N-H) bonding of gCN structure and the π-excitation, respectively.[53] The XPS fitted spectrum of the O 1s (**Figure 7-b**) shows a broad peak located at ~532.34 eV that could be related to the hydroxyl (-OH) groups that might be present at the gCN surface.[49]

Table 1. Summary of the BET-SSA, BJH pore volume, and pore size data of gCN, 5%Au/gCN, and 5%Ag/gCN powder photocatalysts.

Sample	SSA_{BET} (m^2/g)	BJH Pore Volume (cm^3/g)	Pore Size (nm)		
			Adsorption average pore width (4V/A by BET)	BJH Adsorption average pore radius (2V/A)	BJH Desorption average pore radius (2V/A)
gCN	45.02 ± 0.3682	0.644	57.21	27.75	16.29
5%Au/gCN	22.94 ± 0.5779	0.194	33.75	21.20	16.13
5$Ag/gCN	53.23 ± 0.0627	0.499	37.53	17.32	14.36

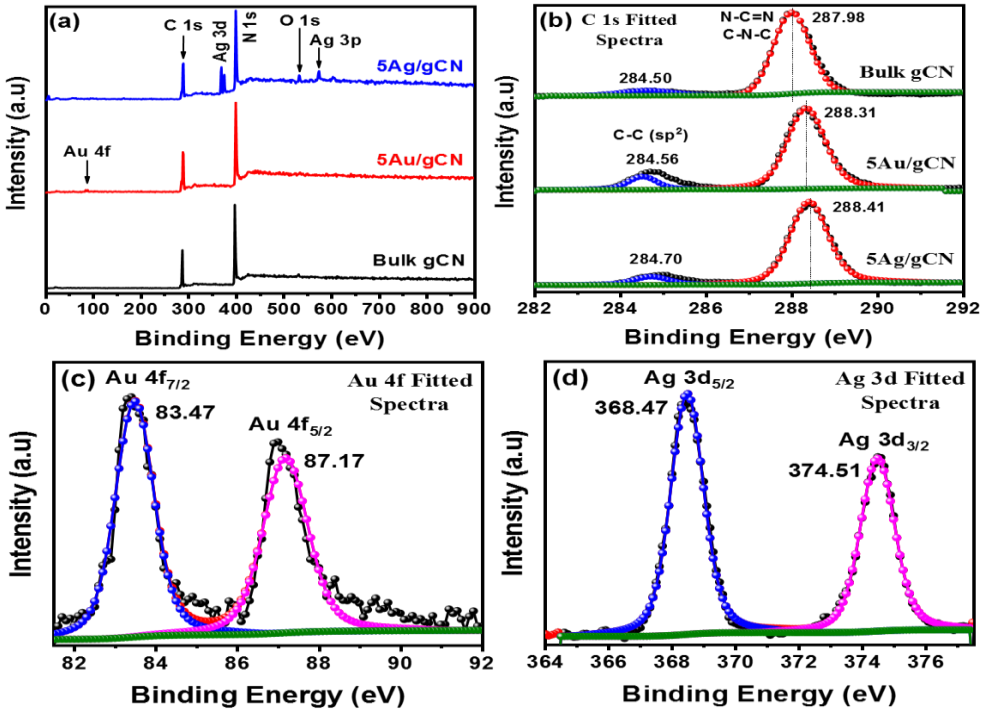

Figure 6. (a) XPS survey spectra of gCN, 5%Au/gCN, and 5%Ag/gCN. **(b-d)** High-resolution scan spectra of **(b)** C 1s of selected samples, **(c)** Au 4f of 5%Au/gCN, and **(d)** Ag 3d of 5%Ag/gCN.

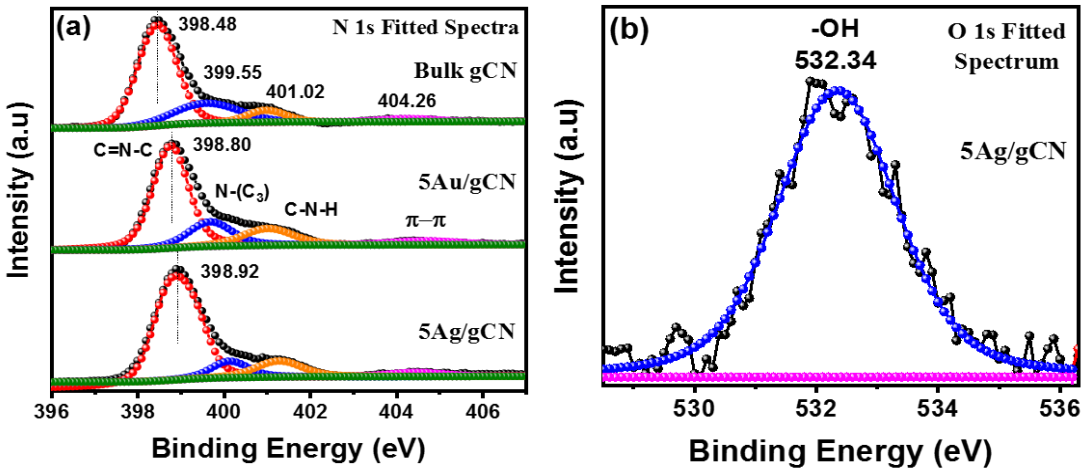

Figure 7. (a,b) High-resolution XPS spectra of **(a)** N 1s of selected samples, and **(b)** O 1s of 5%Ag/gCN sample.

3.4. Photocatalytic Oxidation of Organic Water Pollutants

The photocatalytic activity of the *x*%Au/gCN and *x*%Ag/gCN photocatalysts for photooxidation of organic water pollutants under visible light irradiation was evaluated and compared to that of pristine gCN. The photocatalytic efficiency of the different catalysts was studied toward the photooxidation of MO (10 mg/L) and RB (20 mg/L) dyes for different irradiation times. The performance of prepared samples was quantified by the determination of the quantity degraded of dyes during the dark incubation and photooxidation process. It is known that the performance of a photocatalyst increases with increasing of the quantity adsorbed of a given pollutant and hence reduces the time needed for photooxidation of pollutants.[54] In a typical photocatalytic experiment, the adsorption-desorption equilibrium was set to 60 min in dark for all experiments. A 300 W Xe lamp with a UV cutoff filter (λ >500 nm) was used for the visible light irradiation. The photooxidation percentage was determined using UV-visible spectrophotometric measurements. The intensity was taken at the wavelength of the maximum absorption (λ_{max}) at 464 nm for MO and 549 nm for RB. In all cases, a control experiment for each studied pollutant was also performed to evaluate the photooxidation performance without the use of photocatalyst powder.

Figure 7 presents the plots of C/C_0 vs time for photooxidation of MO and RB over gCN, *x*%Au/gCN, and *x*%Ag/gCN photocatalysts under visible light irradiation. It also shows the plots of C/C_0 vs. time of photooxidation of MO over different catalyst loading of 5%Ag/gCN, in addition to photooxidation of MO and RB of different solution densities. As can be seen in **Figure 7-a,b**, the gCN, *x*%Au/gCN, and *x*%Ag/gCN photocatalysts displayed varied adsorption ability and photocatalytic performance toward MO (**Figure 7-a**) and RB (**Figure 7-b**) in dark and under visible light irradiation. The curves shown in **Figure 7-a** indicate that the 2%Au/gCN and 5%Au/gCN hybrid photocatalysts resulted in adsorptive removal of about 3.87 % and 11.80 % of MO compared to 11.52 % for gCN within 1 h in dark. On the other hand, the adsorption abilities in the cases of 2%Ag/gCN and 5%Ag/gCN hybrids were significantly improved and adsorptive removal of 66.45% and 85.33% of MO could be achieved within 1 h in dark, respectively. Similarly, the 2%Ag/gCN and 5%Ag/gCN hybrids exhibited an extraordinary adsorption ability toward RB (20 mg/L) compared to the gCN and *x*%Au/gCN hybrids after 1 h in dark, as can be seen in **Figure 7-b**. The gCN and *x*%Au/gCN hybrids demonstrated a lower adsorption capacity of about 14 % for RB compared to the 2%Ag/gCN and 5%Ag/gCN hybrids which effectively removed 86.63 % and 97 % of RB in dark, respectively.

As mentioned before, the adsorption ability of a photocatalyst toward a given pollutant is an important parameter that can affect its photocatalytic performance. The photocatalysts possessing good adsorption abilities can exhibit improved photocatalytic activity and hence photooxidation at lower irradiation. Based on the above findings, the plots in **Figure 7-a** showed that only 33.55% of MO were photodegraded in presence of both 2%Au/gCN and 5%Au/gCN hybrids compared to 55.33% in the case of pristine gCN within 60 min of visible light irradiation, respectively. On the other hand, the 2% and 5%Ag/gCN photocatalysts (**Figure 7-a**) exhibited a superior photocatalytic performance toward MO photooxidation in a much shorter time of visible light irradiation. The 2%Ag/gCN hybrid photocatalyst caused photodegradation of about 86.50% of MO within 20 min of visible light irradiation. Whereas the 5%Ag/gCN hybrid photocatalyst exhibited a superior performance with complete photooxidation of MO (100%) at the same time of visible light irradiation (20 min). In the case of RB photooxidation (**Figure 7-b**), both 2%Au/gCN and 5%Au/gCN hybrids resulted in photodegradation of 100% and 96.41% of RB, respectively, compared to 72.54% in the case of gCN within 40 min of visible light irradiation. Whereas the irradiation time needed to achieve complete photooxidation of RB (100%) was decreased to 15 min only over both 2%Ag/gCN and 5%Ag/gCN hybrid systems.

The enhanced photocatalytic activity of the Ag/gCN hybrid photocatalysts reduced the irradiation time needed for complete photooxidation of MO and RB. This can be attributed to the improved adsorption ability of Ag/gCN systems compared to Au/gCN systems toward MO and RB in dark. The adsorption of dye molecules onto a given

adsorbent surface relies on the electrostatic interactions between the dye and the catalyst surface. In the case of gCN-based catalysts, the interaction between the conjugated domain of the adsorbent material and the π-π system of dye molecules is also important.[54] The zeta potential measurements of the aqueous solutions of gCN, 5%Au/gCN, and 5%Ag/gCN samples were performed at neutral pH to understand the origin of their adsorption and photocatalytic properties. The values of zeta potential of the as-prepared gCN and 5%Au/gCN were -31 mV and -15 mV at neutral pH, respectively. While the 5%Ag/gCN hybrid aqueous solutions possessed an average zeta potential value of +11.7 mV at neutral pH. It can be noticed that after Au NPs photodeposition the net negative charge on the surface was decreased to -15 mV. In the case of photodeposited Ag NPs, the surface of Ag/gCN expresses a net positive charge on the surface. The MO and RB dyes are anionic compounds with main negative charges at neutral pH. Hence, the results of the adsorptive and photocatalytic removal of the organic dyes over MNPs/gCN can be understood based on the electrostatic interaction between catalysts and organic pollutant molecules. The net surface charge of gCN and 5%Au/gCN hybrid were mainly negative (-31 mV and -15 mV) and results in an electrostatic repulsion with MO and RB molecules which bear net negative charge also. The net positive charge on the surface of the 5%Ag/gCN causes strong electrostatic interactions with the MO and RB molecules and this leads to increased adsorption of the two dyes. Thus, the enhanced adsorption and visible light absorption of the MNPs/gCN improved the photocatalytic properties and increased the photogenerated charge density resulting in overall higher performance of MNPs/gCN than pristine gCN.[20]

The effect of the catalyst loading on photocatalytic performance has been studied to reveal the optimal dosage of the photocatalyst for the photooxidation reaction. **Figure 7-c** shows the plots of C/C_0 vs time for photooxidation of MO over 5%Ag/gCN using different catalyst loading of 20 mg, 60 mg, and 100 mg. The plots indicate that the quantities adsorbed of MO over the 5%Ag/gCN were 17.72%, 58%, and 85.37% using 20 mg, 60 mg, and 100 mg of catalyst dosage, respectively. The increase of the catalyst loading is associated with an increase in adsorption with can be ascribed to the increased number of active sites on the catalyst surface. Consequently, the highest photocatalytic activity was observed using catalyst loading of 100 mg as discussed earlier where the increased active site density can lead to an increased rate of hydroxyl radical production during the photooxidation process.[1] **Figure 7-d** shows the photocatalytic performance of 5%Ag/gCN toward the degradation of higher concentrations of MO (20 mg/L) and RB (40 mg/L) under visible light irradiation. The 5%Ag/gCN with catalyst loading of 1mg/ml led to photodegradation of 100% of MO (20 mg/L) within 120 min of visible light irradiation. On the other hand, the complete photooxidation of RB (40 mg/L) was achieved within 30 min of visible light exposure over the same catalyst with lower loading of 0.5mg/ml. This indicates that the 5%Ag/gCN hybrid still maintains its photocatalytic performance even at a high concentration of organic water pollutants.

3.5. Optical Characteristics and the Photocatalytic Performance

Studying the electronic and optical properties of the prepared materials is necessary to understand their photoactivity and the origin of their photocatalytic activity. Hence, the DRS and PL spectral properties of the different catalysts were studied. **Figure 8** displays the UV-vis DRS and PL spectra of different catalysts including gCN, *x*%Au/gCN, and *x*%Ag/gCN. As shown in **Figure 8-a**, the DRS spectrum of the gCN displays an optical absorption in the range from 250 to 450 nm, similar to a typical absorption spectrum of semiconductors. The absorption spectrum of gCN is featured with two DRS absorption bands at ~325 nm and ~370 nm due to the UV light sensitivity of the gCN. Additionally, gCN possesses a slightly visible light absorption band in the range of 420 to 500 nm. The MNPs/gCN exhibited higher visible light absorption compared to gCN owing to the enhanced absorption caused by the MNPs (**Figure 8-a**). The 2%Au/gCN and 5%Au/gCN hybrid photocatalysts exhibited strong absorption bands at 540 nm and 555 nm alongside the two bands of the gCN in the UV range (**Figure 8-a**). These prominent absorption bands in the visible range are ascribed to the intrinsic surface plasmon resonance (SPR) effect of the MNPs.[41, 55] Moreover, increasing the metal loading from 2% to 5% caused a slight red-shift of the DRS absorption

peaks.[55] Similarly, the DRS spectra of the 2%Ag/gCN and 5%Ag/gCN hybrids showed small absorption bands at ~475 nm and ~490 nm which is due to the SPR effect of Ag NPs.[31] The obtained results reveal the evident anchoring of the MNPs onto the gCN surface. Consequently, the increased light absorption could increase the density of the photogenerated charged species leading to enhanced photocatalytic performance under visible light irradiation.

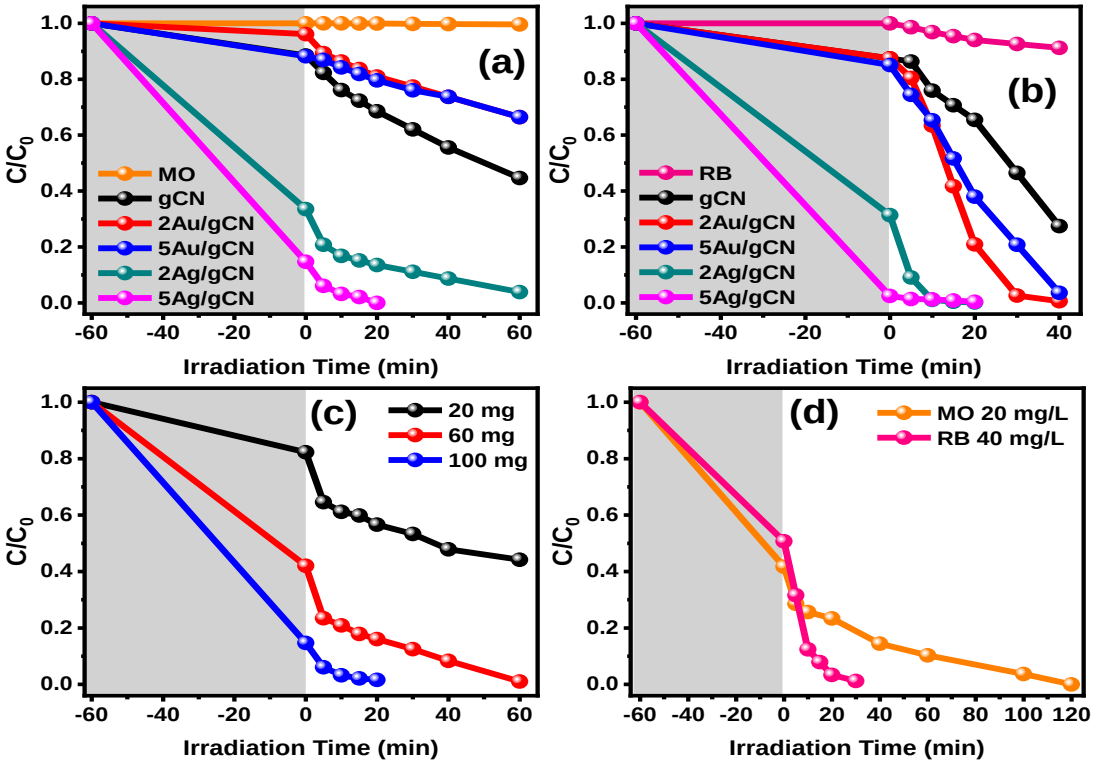

Figure 7. (a,b) Plots of C/C_0 vs time for photooxidation of **(a)** MO and **(b)** RB over gCN, *x*%Au/gCN, and *x*%Ag/gCN catalysts under visible light irradiation. **(c,d)** Plots of C/C_0 vs. time of photooxidation over 5%Ag/gCN for **(c)** MO (10 mg/L) using different catalyst loading, and **(d)** MO (20 mg/L, 100 ml, 100 mg catalyst) and RB (40 mg/L, 100 ml, 50 mg catalyst).

The photoluminescence of such materials stems from the emission of light upon the recombination of the photogenerated charges including electrons and holes. Also, it is well-known that the efficiency of such a photocatalyst is corresponding to the effective separation of the electron and hole pairs.[56] Therefore, the obtained emission can help define the efficiency of the electrons/holes transfer, trapping, immigration, and separation. **Figure 8-b** presents the PL spectra of the gCN, *x*%Au/gCN, and *x*%Ag/gCN recorded using an excitation wavelength of 360 nm. As can be seen in **Figure 8-b**, the PL spectrum of the gCN shows a strong emission peak centered at ~470 nm which is ascribed to light emitted after recombination of the electron and hole pairs in the conduction band (CB) and valance band (VB) of gCN.[55, 56] Also, the PL emission spectra of the *x*%Au/gCN and *x*%Ag/gCN hybrids exhibited emission peaks similar to that observed in the case of the pure counterparts. In the case of the *x*%Au/gCN and *x*%Ag/gCN hybrids, the coupling of gCN and MNPs (Au NPS or Ag NPs) lowered the emission intensity compared to gCN. The recombination of the photogenerated charges causes emission as PL, and hence lowering the recombination can decrease the PL intensity. For the MNPs/gCN hybrids, the existence of the metal ions (Au or Ag) could improve the interfacial charge transfer of the photogenerated electrons and holes resulting in overall decreased emission intensity of MNPs/gCN hybrids compared to gCN. This confirms the effect of the metals in trapping the charges and thus inhibiting their recombination. Therefore, the density of photogenerated charges is increased improving the photocatalytic performance of the MNPs/gCN systems.[56] The overall DRS and Pl spectral results

revealed the increased absorption in the visible region and the diminished emission of the MNPs/gCN hybrid photocatalysts, which explains their improved photocatalytic performance compared to gCN.

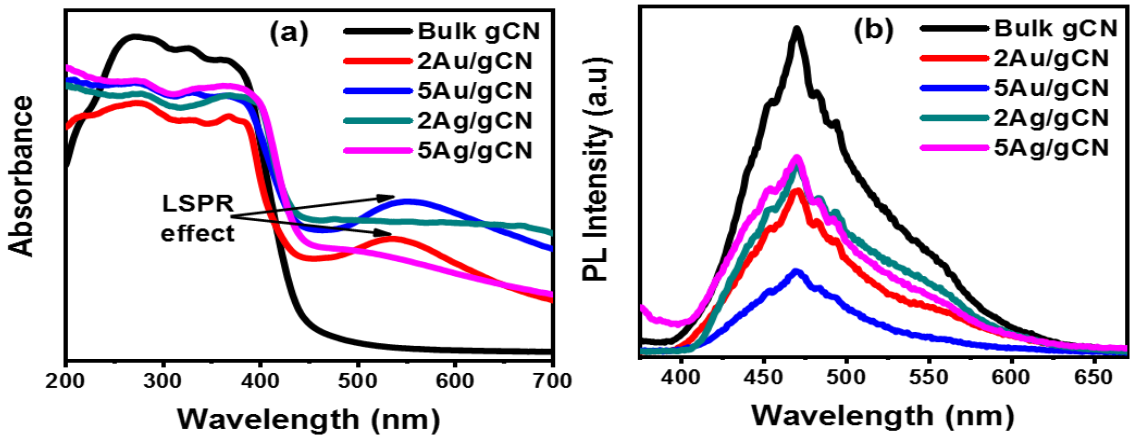

Figure 8. (a) Diffuse reflectance spectroscopy (DRS) and **(b)** photoluminescence (PL) spectra of the prepared catalysts.

3.6. Photoelectrochemical (PEC) Measurements

The photoelectrochemical (PEC) measurements are helpful to understand the charge separation and transfer processes. The PEC properties were studied by investigating the electrochemical impedance spectroscopy (EIS) and photocurrent response characteristics of selected photocatalysts, namely gCN and 5%Ag/gCN. All experiments were conducted using an aqueous solution of sodium sulfate (0.5 M) under a 150W Xe lamp with a UV cut-off filter. The EIS Nyquist spectra and the transient photocurrent responses of gCN and 5%Ag/gCN photocatalysts are displayed in **Figure 9**. The EIS Nyquist spectra of the gCN and 5%Ag/gCN hybrid in dark and under visible light irradiation are shown in **Figure 9-a**. The EIS Nyquist spectrum of the 5%Ag/gCN hybrid exhibited a smaller arc radius compared to pristine which indicates a faster rate of the interfacial charge transfer and thus lowered the electron transfer resistance over the photoelectrode surface under visible light irradiation.[57]

Furthermore, the transient photocurrent responses of the gCN and 5Ag/gCN were investigated by applying several on-off cycles of the visible light irradiation. As shown in **Figure 9-b**, the photocurrent response of the 5%Ag/gCN hybrid was higher than that of gCN, which reveals the enhanced separation efficiency of the photogenerated electron and hole pairs. Moreover, all selected samples exhibited stable photocurrent response for a total of nine on-off cycles under shopped-irradiation with 30 s interval time, indicating that all samples express good photoelectrochemical stability. The improved photocurrent response confirms the evident charge transfer and the interfacial interaction between the Ag NPs and gCN.[11, 57] Overall, the photocurrent response results are consistent with the EIS Nyquist analysis and PL characteristics. This indicates that the 5%Ag/gCN hybrid possessed the highest charge separation and charge transfer efficiencies of the photogenerated charged species, and it is favorable to enhance the photocatalytic activity.

3.7. Mechanistic Photooxidation Steps

An efficient photocatalyst shall meet some fundamental criteria associated with the optical band-gap energy and the position of the bandgap. The bandgap energy is indicative of the wavelengths that a semiconductor can absorb. Also, the optical bandgap position affects the direction of the charge transfer.[58] The photogeneration and separation of the charged species at the interface of a semiconductor and the photostability also affect the photo-redox process.[6] As discussed above, the 5%Ag/gCN hybrid photocatalyst exhibited superior photocatalytic performance compared to gCN and other prepared catalysts. This result can be ascribed to the synergistic effect of the MNPs leading to enhanced visible light harvesting alongside a smaller bandgap of hybrid photocatalysts with the

corresponding increase in the MNPs content. A sketch of the photooxidation steps including the charge generation, separation, and transfer within the 5%Ag/gCN composite photocatalyst is depicted in **Figure 10**. The 5%Ag/gCN hybrid has a smaller bandgap of about 2.66 eV relative to gCN (~2.7 eV) with a slightly higher ability to absorb visible light. The 5%Ag/gCN absorbs visible light photons with subsequent photogeneration of charged species as in gCN also. The electrons (e^-) generated in the CB of gCN after absorption of light can rapidly be transferred to the CB of the Ag NPs through interfacial charge transfer due to their intimate interfacial contact.[58] These electrons could combine with oxygen (O_2) molecules to produce superoxide radicals ($O_2^{\cdot-}$) which can combine with H^+ and produce hydrogen peroxide (H_2O_2).[59] Additionally, due to the low band-gap of the gCN, the photogenerated holes (h^+) may interact with the hydroxyl groups (OH^-) or water (H_2O) molecules adsorbed on the surface to form reactive hydroxyl radicals ($OH^{\cdot}$).[21] The reactivity and strong oxidizing power of the ($O_2^{\cdot-}$), (H_2O_2), and ($OH^{\cdot}$) can mediate the photooxidation of the organic water pollutants.[21, 57] The trapping of the h^+ in the VB of gCN and trapping of e^- injected from CB of gCN to the CB of Ag NPs could effectively induce the charge carriers separation and thus delay the recombination of the electrons-holes (e^-/h^+) pairs. This led to improving the photocatalytic performance of MNPs/gCN hybrids toward the photooxidation of water pollutants.

3.8. The Catalyst Reusability

Besides the superior photocatalytic efficiency of the prepared hybrids, the photostability and reusability of the 5%Ag/gCN hybrid photocatalyst were further evaluated for economic considerations. **Figure 11** presents a plot of the cycling stability of 5%Ag/gCN for photooxidation of MO (10 mg/L) under visible light irradiation for 3 cycles (80 min). The 5%Ag/gCN exhibited an excellent and stable photooxidation activity for three successive cycles of reaction (cyc. 1=20 min, cyc. 2=30 min, cyc. 3= 30 min; total time = 80 min). Moreover, after the third cycle, the photooxidation rate of MO over the 5%Ag/gCN surface was retained at 95% after 80 min of visible light irradiation. This slight decrease in photocatalytic activity might be due to the losses of the photocatalyst powder during the desorption process. This result indicates the good photostability and reusability of the prepared 5%Ag/gCN hybrid.

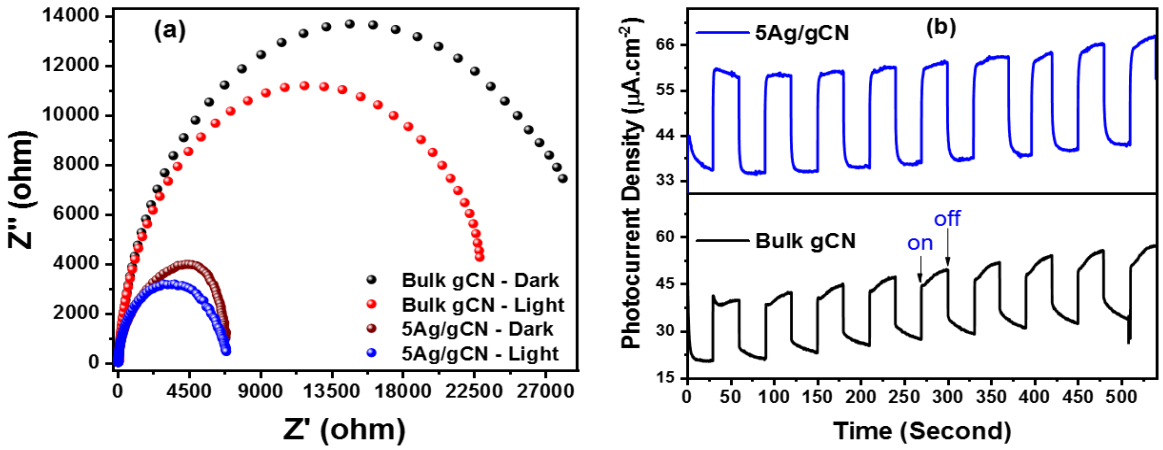

Figure 9. **(a)** EIS Nyquist spectra and **(b)** Transient photocurrent responses of gCN and 5%Ag/gCN photocatalysts.

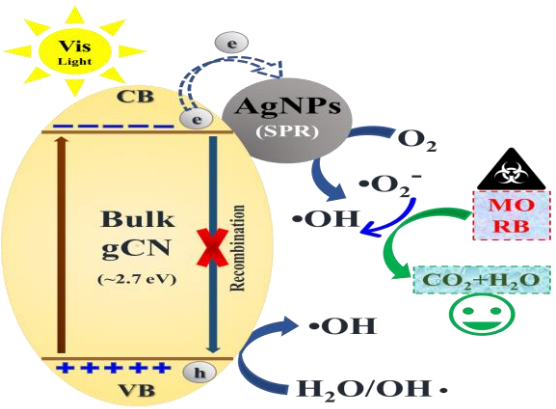

Figure 10. A sketch of the elementary steps representing the charge generation, separation, and transfer within Ag/gCN hybrid photocatalyst leading to photooxidation of dye molecules.

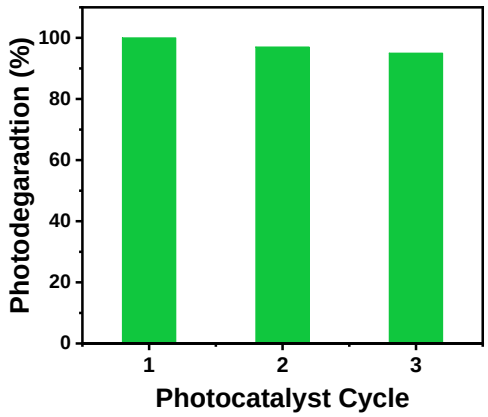

Figure 11. A plot displaying the cycling stability of 5%Ag/gCN for photooxidation of MO (10 mg/L) under visible light irradiation for 3 cycles (80 min).

4. Conclusions

The photocatalytic degradation of hazardous water pollutants is a vital aim to secure safe and clean water. Photocatalysis provides promising technology for the utilization of various photocatalysts and clean energy toward achieving this goal. Herein, we report on the facile synthesis of visible light-sensitive photocatalysts of metal nanoparticles/ graphitic carbon nitride with enhanced photocatalytic activity for water treatment. For the sake of comparison, gold and silver nanoparticles anchored onto gCN were synthesized by sonodispersion and in-situ photodeposition. The performance of the catalysts was evaluated for the degradation of example organic pollutants including MO and RB. The effect of the metal nanoparticles on the photocatalytic efficiency of gCN and MNPs/gCN was studied by changing the metallic ratio in the prepared catalysts. To study the structure and properties of the prepared catalysts, samples were characterized using TEM, SEM, XRD, FTIR, BET surface area, XPS, UV-vis DRS, and PL spectroscopy. The prepared catalysts were utilized for the photocatalytic degradation of different organic water pollutants under visible light irradiation, it was possible to confirm the promoting effect of MNPs with the appropriate loading ratio which was found to improve the optical properties and photocatalytic performance of the material for pollutants photooxidation. The results revealed that the type of MNPs as a co-catalytic over the gCN surface plays a vital role in promoting photocatalytic activity. The obtained results exhibit the superior performance of the Ag/gCN hybrid photocatalysts compared to gCN or Au/gCN hybrid systems. The highest photocatalytic degradation of MO and RB pollutants was achieved in the presence of a 5%Ag/gCN hybrid photocatalyst under visible light irradiation (100 mW.cm^{-2}). The PEC properties of 5%Ag/gCN further confirmed the improved visible light harvesting and the delayed recombination rate of the photogenerated charged species compared to pure counterparts. In conclusion, the utilization of solar energy via using the effective photocatalyst system for the photooxidation of water pollutants can have immense benefits environmentally and economically.

5. Acknowledgments

This work was supported by IMRE (A*STAR Research Attachment Programme (ARAP), Project# SC25/18-8R1312, Singapore) and NILES (Internal Funds, Cairo University, Egypt). The authors thank Ms. Siew Yee Wong (IMRE) for her help with the TEM imaging. Mostafa Zedan and Abdallah F. Zedan are dedicating this work in memory of their dad, Fathy Zedan, who recently passed away.

6. References

1. Zhang, S., et al., *Recent developments in fabrication and structure regulation of visible-light-driven g-C3N4-based photocatalysts towards water purification: A critical review.* Catalysis Today, 2019. **335**: p. 65-77.
2. Cao, S., et al., *Polymeric Photocatalysts Based on Graphitic Carbon Nitride.* Advanced Materials, 2015. **27**(13): p. 2150-2176.
3. Lam, S.-M., J.-C. Sin, and A.R. Mohamed, *A review on photocatalytic application of g-C3N4/semiconductor (CNS) nanocomposites towards the erasure of dyeing wastewater.* Materials Science in Semiconductor Processing, 2016. **47**: p. 62-84.

4. Wang, Z., et al., *Highly regenerable alkali-resistant magnetic nanoparticles inspired by mussels for rapid selective dye removal offer high-efficiency environmental remediation.* Journal of Materials Chemistry A, 2015. **3**(39): p. 19960-19968.
5. Aoudj, S., et al., *Electrocoagulation process applied to wastewater containing dyes from textile industry.* Chemical Engineering and Processing: Process Intensification, 2010. **49**(11): p. 1176-1182.
6. Mersal, M., G.G. Mohamed, and A.F. Zedan, *Promoted visible-light-assisted oxidation of methanol over N-doped TiO2/WO3 nanostructures.* Optical Materials, 2021: p. 111810.
7. Luo, J., et al., *A Critical Review on Energy Conversion and Environmental Remediation of Photocatalysts with Remodeling Crystal Lattice, Surface, and Interface.* ACS Nano, 2019. **13**(9): p. 9811-9840.
8. Jiang, L., et al., *Doping of graphitic carbon nitride for photocatalysis: A reveiw.* Applied Catalysis B: Environmental, 2017. **217**: p. 388-406.
9. Kumar, S.G. and K.S.R.K. Rao, *Comparison of modification strategies towards enhanced charge carrier separation and photocatalytic degradation activity of metal oxide semiconductors (TiO2, WO3 and ZnO).* Applied Surface Science, 2017. **391**: p. 124-148.
10. Reddy, K.R., et al., *Polymeric graphitic carbon nitride (g-C3N4)-based semiconducting nanostructured materials: Synthesis methods, properties and photocatalytic applications.* Journal of Environmental Management, 2019. **238**: p. 25-40.
11. Hu, J., et al., *Metal-free heterojunction of black phosphorus/oxygen-enriched porous g-C3N4 as an efficient photocatalyst for Fenton-like cascade water purification.* Journal of Materials Chemistry A, 2020. **8**(37): p. 19484-19492.
12. Sudhaik, A., et al., *Review on fabrication of graphitic carbon nitride based efficient nanocomposites for photodegradation of aqueous phase organic pollutants.* Journal of Industrial and Engineering Chemistry, 2018. **67**: p. 28-51.
13. Zedan, M., et al., *Visible-light active metal nanoparticles@carbon nitride for enhanced removal of water organic pollutants.* Journal of Environmental Chemical Engineering, 2022. **10**(3): p. 107780.
14. Gogoi, D., et al., *Silver grafted graphitic-carbon nitride ternary hetero-junction Ag/gC3N4(Urea)-gC3N4(Thiourea) with efficient charge transfer for enhanced visible-light photocatalytic green H2 production.* Applied Surface Science, 2021. **558**: p. 149900.
15. Kim, J.S., J.W. Oh, and S.I. Woo, *Improvement of the photocatalytic hydrogen production rate of g-C3N4 following the elimination of defects on the surface.* Catalysis Today, 2017. **293-294**: p. 8-14.
16. Fu, J., et al., *Hierarchical Porous O-Doped g-C3N4 with Enhanced Photocatalytic CO2 Reduction Activity.* Small, 2017. **13**(15): p. 1603938.
17. Cheng, N., et al., *Au-Nanoparticle-Loaded Graphitic Carbon Nitride Nanosheets: Green Photocatalytic Synthesis and Application toward the Degradation of Organic Pollutants.* ACS Applied Materials & Interfaces, 2013. **5**(15): p. 6815-6819.
18. Fu, Y., et al., *Ag/g-C3N4 catalyst with superior catalytic performance for the degradation of dyes: a borohydride-generated superoxide radical approach.* Nanoscale, 2015. **7**(32): p. 13723-13733.
19. Zhang, H., et al., *Enhanced photocatalytic performance of boron and phosphorous co-doped graphitic carbon nitride nanosheets for removal of organic pollutants.* Separation and Purification Technology, 2019. **226**: p. 128-137.
20. Katsumata, H., et al., *Highly Efficient Photocatalytic Activity of g-C3N4/Ag3PO4 Hybrid Photocatalysts through Z-Scheme Photocatalytic Mechanism under Visible Light.* Industrial & Engineering Chemistry Research, 2014. **53**(19): p. 8018-8025.
21. Monga, D. and S. Basu, *Enhanced photocatalytic degradation of industrial dye by g-C3N4/TiO2 nanocomposite: Role of shape of TiO2.* Advanced Powder Technology, 2019. **30**(5): p. 1089-1098.
22. Zhang, Z., et al., *Graphitic carbon nitride nanosheet for photocatalytic hydrogen production: The impact of morphology and element composition.* Applied Surface Science, 2017. **391**: p. 369-375.
23. Wang, J., et al., *Facile Gel-Based Morphological Control of Ag/g-C3N4 Porous Nanofibers for Photocatalytic Hydrogen Generation.* ACS Sustainable Chemistry & Engineering, 2017. **5**(11): p. 10633-10639.
24. Song, Y., et al., *Construction of Ag/g-C3N4 photocatalysts with visible-light photocatalytic activity for sulfamethoxazole degradation.*

Chemical Engineering Journal, 2018. **341**: p. 547-555.
25. Xue, J., et al., *A novel synthesis method for Ag/g-C3N4 nanocomposite and mechanism of enhanced visible-light photocatalytic activity.* Journal of Materials Science: Materials in Electronics, 2019. **30**(16): p. 15636-15645.
26. Lin, H., et al., *Facile anion-exchange synthesis of BiOI/BiOBr composite with enhanced photoelectrochemical and photocatalytic properties.* Ceramics International, 2014. **40**(7, Part A): p. 9743-9750.
27. Pradeev raj, K., et al., *Influence of Mg Doping on ZnO Nanoparticles for Enhanced Photocatalytic Evaluation and Antibacterial Analysis.* Nanoscale Research Letters, 2018. **13**(1): p. 229.
28. Jiang, Y., et al., *Facile in-situ Solvothermal Method to synthesize double shell ZnIn2S4 nanosheets/TiO2 hollow nanosphere with enhanced photocatalytic activities.* Ceramics International, 2018. **44**(6): p. 6115-6126.
29. Li, N., et al., *Uniform Fe2O3 nanocubes on BiOCl nanosheets and its improved photocatalytic activity.* Journal of Molecular Catalysis A: Chemical, 2014. **395**: p. 428-433.
30. Maeda, K., R. Abe, and K. Domen, *Role and Function of Ruthenium Species as Promoters with TaON-Based Photocatalysts for Oxygen Evolution in Two-Step Water Splitting under Visible Light.* The Journal of Physical Chemistry C, 2011. **115**(7): p. 3057-3064.
31. Ma, L.L., et al., *The fabrication of SnSe/Ag nanoparticles on TiO2 nanotubes.* Materials Science and Engineering: B, 2013. **178**(1): p. 77-82.
32. Dasgupta, N.P., et al., *Atomic Layer Deposition of Platinum Catalysts on Nanowire Surfaces for Photoelectrochemical Water Reduction.* Journal of the American Chemical Society, 2013. **135**(35): p. 12932-12935.
33. Murata, A., et al., *Visible-Light Active Photocatalytic WO3 Films Loaded with Pt Nanoparticles Deposited by Sputtering.* Journal of Nanoscience and Nanotechnology, 2012. **12**(6): p. 5082-5086.
34. Khan, M.E., M.M. Khan, and M.H. Cho, *Environmentally sustainable biogenic fabrication of AuNP decorated-graphitic g-C3N4 nanostructures towards improved photoelectrochemical performances.* RSC Advances, 2018. **8**(25): p. 13898-13909.
35. Heidari, S., M. Haghighi, and M. Shabani, *Sono-photodeposition of Ag over sono-fabricated mesoporous Bi2Sn2O7-two dimensional carbon nitride: Type-II plasmonic nano-heterojunction with simulated sunlight-driven elimination of drug.* Chemical Engineering Journal, 2020. **389**: p. 123418.
36. Zhu, H., K.-J. Wu, and C.-H. He, *Ultrasound-assisted synthesis of visible-light-driven Ag/g-C3N4 catalysts in a continuous flow reactor.* Chemical Engineering Journal, 2022. **429**: p. 132412.
37. Faisal, M., et al., *Au nanoparticles-doped g-C3N4 nanocomposites for enhanced photocatalytic performance under visible light illumination.* Ceramics International, 2020. **46**(14): p. 22090-22101.
38. Costa, J.M. and A.F.d. Almeida Neto, *Ultrasound-assisted electrodeposition and synthesis of alloys and composite materials: A review.* Ultrasonics Sonochemistry, 2020. **68**: p. 105193.
39. Wenderich, K. and G. Mul, *Methods, Mechanism, and Applications of Photodeposition in Photocatalysis: A Review.* Chemical Reviews, 2016. **116**(23): p. 14587-14619.
40. Volokh, M. and T. Mokari, *Metal/semiconductor interfaces in nanoscale objects: synthesis, emerging properties and applications of hybrid nanostructures.* Nanoscale Advances, 2020. **2**(3): p. 930-961.
41. Colmenares, J.C., et al., *Sonophotodeposition of Bimetallic Photocatalysts Pd–Au/TiO2: Application to Selective Oxidation of Methanol to Methyl Formate.* ChemSusChem, 2015. **8**(10): p. 1676-1685.
42. Magdziarz, A., et al., *Iron-Containing Titania Photocatalyst Prepared by the Sonophotodeposition Method for the Oxidation of Benzyl Alcohol.* ChemCatChem, 2016. **8**(3): p. 536-539.
43. Jodeyri, M., M. Haghighi, and M. Shabani, *Plasmon-assisted demolition of antibiotic using sono-photoreduction decoration of Ag on 2D C3N4 nanophotocatalyst enhanced with acid-treated clinoptilolite.* Ultrasonics Sonochemistry, 2019. **54**: p. 220-232.
44. Song, J., et al., *Synthesis of Au/Graphene Oxide Composites for Selective and Sensitive Electrochemical Detection of Ascorbic Acid.* Scientific Reports, 2014. **4**(1): p. 7515.
45. Lee, K.-J., et al., *Synthesis of silver nanoparticles using cow milk and their antifungal activity against phytopathogens.* Materials Letters, 2013. **105**: p. 128-131.
46. El-Ella Hussein Gad, A.A., et al., *Synthesis of High Efficient CS/PVDC/TiO2-Au Nanocomposites for Photocatalytic Degradation of Carcinogenic Ethidium Bromide*

in Sunlight. Egyptian Journal of Chemistry, 2020. **63**(5): p. 1619-1638.
47. Farid, S., et al., *Exploring ATR Fourier transform IR spectroscopy with chemometric analysis and laser scanning microscopy in the investigation of forensic documents fraud.* Optics & Laser Technology, 2021. **135**: p. 106704.
48. Zedan, A.F., et al., *Coupling ATR-FTIR Spectroscopy and Chemometric Analysis for Rapid and Non-Destructive Ink Discrimination of Forensic Documents.* Egyptian Journal of Chemistry, 2022.
49. Paul, D.R., et al., *ZnO-Modified g-C3N4: A Potential Photocatalyst for Environmental Application.* ACS Omega, 2020. **5**(8): p. 3828-3838.
50. Basina, G., et al., *Ultrasmall Metal-Doped CeO2 Nanoparticles for Low-Temperature CO Oxidation.* ACS Applied Nano Materials, 2020. **3**(11): p. 10805-10813.
51. Polychronopoulou, K., et al., *Design Aspects of Doped CeO2 for Low-Temperature Catalytic CO Oxidation: Transient Kinetics and DFT Approach.* ACS Applied Materials & Interfaces, 2021. **13**(19): p. 22391-22415.
52. Zedan, A.F., et al., *CO Oxidation at Near-Ambient Temperatures over TiO2-Supported Pd-Cu Catalysts: Promoting Effect of Pd-Cu Nanointerface and TiO2 Morphology.* Nanomaterials, 2021. **11**(7).
53. Qin, J., et al., *Improving the photocatalytic hydrogen production of Ag/g-C3N4 nanocomposites by dye-sensitization under visible light irradiation.* Nanoscale, 2016. **8**(4): p. 2249-2259.
54. Bhowmik, T., M.K. Kundu, and S. Barman, *Ultra small gold nanoparticles–graphitic carbon nitride composite: an efficient catalyst for ultrafast reduction of 4-nitrophenol and removal of organic dyes from water.* RSC Advances, 2015. **5**(48): p. 38760-38773.
55. Patnaik, S., D.P. Sahoo, and K. Parida, *Photo-catalytic H2 evolution over Au modified mesoporous g-C3N4.* Materials Today: Proceedings, 2021. **35**: p. 247-251.
56. Zhu, Z., et al., *Fabrication of conductive and high-dispersed Ppy@Ag/g-C3N4 composite photocatalysts for removing various pollutants in water.* Applied Surface Science, 2016. **387**: p. 366-374.
57. Liu, R., et al., *Ag-Modified g-C3N4 Prepared by a One-Step Calcination Method for Enhanced Catalytic Efficiency and Stability.* ACS Omega, 2020. **5**(31): p. 19615-19624.
58. He, Q., et al., *Enhancement of photocatalytic and photoelectrocatalytic activity of Ag modified Mpg-C3N4 composites.* Applied Surface Science, 2017. **391**: p. 423-431.
59. Yang, Y., et al., *Ti3C2 Mxene/porous g-C3N4 interfacial Schottky junction for boosting spatial charge separation in photocatalytic H2O2 production.* Applied Catalysis B: Environmental, 2019. **258**: p. 117956.